Investigating the local structure of *B*-site cations in (1-*x*)$BaTiO_3$–*x*$BiScO_3$ and (1-*x*)$PbTiO_3$–*x*$BiScO_3$ using X-ray absorption spectroscopy

Peter E. R. Blanchard

Canadian Light Source, Saskatoon, SK, S7N 2V3, Canada

Andrew P. Grosvenor*

Department of Chemistry, University of Saskatchewan, Saskatoon, SK, S7N 5C9

Abstract

The structural properties of (1-*x*)$BaTiO_3$–*x*$BiScO_3$ and (1-*x*)$PbTiO_3$–*x*$BiScO_3$ were investigated using powder X-ray diffraction and X-ray absorption spectroscopy. Diffraction measurements confirmed that substituting small amounts of $BiScO_3$ into $BaTiO_3$ initially stabilizes a cubic phase at $x = 0.2$ before impurity phases begin to form at $x = 0.5$. $BiScO_3$ substitution also resulted in noticeable changes in the local coordination environment of Ti^{4+}. X-ray absorption near-edge spectroscopy (XANES) analysis showed that replacing Ti^{4+} with Sc^{3+} results in an increase in the off-centre displacement of Ti^{4+} cations. Surprisingly, $BiScO_3$ substitution has no effect on the displacement of the Ti^{4+} cation in the (1-*x*)$PbTiO_3$–*x*$BiScO_3$ solid solution.

Key Words: perovskites, ferroelectrics, scandium, XANES

* Author to whom correspondence should be addressed
E-mail: andrew.grosvenor@usask.ca
Phone: (306) 966-4660

1. Introduction

ABO_3-based perovskite solid solutions, particularly $PbTi_{1-x}Zr_xO_3$, are used extensively in ferroelectric and piezoelectric devices.[1-4] $PbTi_{1-x}Zr_xO_3$ materials exhibit a large piezoelectric coefficient, large coupling factor, high Curie temperature ($T_c \sim 623$ K), and high operating temperature near the morphotropic phase boundary, a region of the $PbTi_{1-x}Zr_xO_3$ solid solution where two ferroelectric phases (tetragonal and rhombohedral) co-exist.[5,6] A distinguishing feature of these two phases is the off-centre displacement of the *B*-site (i.e. Ti^{4+}/Zr^{4+}) cations. This has led to considerable interest in understanding how the local structure of $PbTi_{1-x}Zr_xO_3$ varies with composition as a means of tailoring its electronic properties. This interest has extended to lead-free or reduced-lead alternatives to $PbTi_{1-x}Zr_xO_3$ in recent years because of the adverse environmental effects of lead-containing materials.[7,8] Currently, the most widely used lead-free ferroelectric perovskite is $BaTiO_3$.[9] However, its use is limited by a low Curie temperature. A promising method of developing alternatives to $PbTi_{1-x}Zr_xO_3$ is to replace Pb^{2+} with isoelectronic Bi^{3+}.[9] The (1-*x*)$PbTiO_3$–*x*$BiMeO_3$ (Me^{3+} = Sc, In, Y, Yb, Ga) perovskite materials, particularly (1-*x*)$PbTiO_3$–*x*$BiScO_3$, have been identified as promising alternatives for $PbTi_{1-x}Zr_xO_3$[10-17]

$PbTiO_3$ adopts a tetragonally-distorted perovskite structure in space group *P4mm* at room temperature.[10] The tetragonal *P4mm* perovskite phase is similar to that of the ideal cubic perovskite structure (space group $Pm\bar{3}m$) except that the Ti^{4+} cation (i.e. *B*-site cation) is displaced along the z-direction (Figure 1). The displacement of the Ti^{4+} cation is believed to be an important contributor to the ferroelectric behaviour observed in $PbTiO_3$.[18] The (1-*x*)$PbTiO_3$–*x*$BiScO_3$ solid solution forms the tetragonal *P4mm* phase at $0 \leq x \leq 0.34$. A morphotropic phase boundary (MPB) is observed at $0.34 \leq x \leq 0.36$ in (1-*x*)$PbTiO_3$–*x*$BiScO_3$ consisting of the ferroelectric tetragonal *P4mm* and rhombohedral *R3m* perovskite phases. In the rhombohedral *R3m* phase, the *B*-site cations are displaced the <111> direction (see Figure 1).

Only the rhombohedral *R3m* phase is stable between at $0.36 \leq x \leq 0.5$. The $(1\text{-}x)PbTiO_3$–$xBiScO_3$ is not stable under normal reaction conditions at $x > 0.5$. However, $BiScO_3$ was found to form a monoclinc *C2/c* perovskite phase under high pressures.[19]

Surprisingly, $BiScO_3$ substitution does not enhance the ferroelectric properties of $BaTiO_3$. $BaTiO_3$ forms the ferroelectric tetragonal *P4mm* phase at room temperature. The displacement of that Ti^{4+} has been suggested as being influenced by a pseudo Jahn-Teller effect resulting from the mixing of the HOMO (O t_{1u} and t_{2u}) and LUMO (Ti t_{2g}) states.[20] The tetragonal *P4mm* phase forms in the $(1\text{-}x)BaTiO_3$–$xBiScO_3$ solid solution at $0 \leq x \leq 0.05$. The ferroelectric response is slowly repressed until a relaxor ferroelectric rhombohedral *R3m* perovskite phase forms.[21,22] Both the ferroelectric tetragonal *P4mm* and relaxor ferroelectric rhombohedral *R3m* phases were found to coexists at $0.05 \leq x \leq 0.2$. Unlike normal ferroelectrics, relaxor ferroelectrics show diffuse phase transitions, strong frequency dependency, and weak remnant polarization.[23] The relaxor ferroelectric behaviour in perovskite materials is believed to be due to local cation disorder.[24] The $(1\text{-}x)BaTiO_3$–$xBiScO_3$ solid solution is stable up to $x = 0.6$, where the cubic $Pm\bar{3}m$ perovskite phase forms at $0.2 \leq x \leq 0.6$.

It is generally difficult to measure changes in the local structure of perovskite materials using traditional X-ray diffraction (XRD) techniques as XRD is more sensitive to global symmetry changes. X-ray absorption near-edge spectroscopy (XANES) is sensitive to cation displacement, particularly in Ti-based perovskites.[25-29] For example, XANES has been used to detect subtle differences in the off-centre displacement of the Ti^{4+} and Zr^{4+} cations in $(Bi_{0.5}Na_{0.5})Ti_{1-x}Zr_xO_3$, $BaTi_{1-x}Zr_xO_3$, and $(Bi_{0.5}K_{0.5})Ti_{1-x}Zr_xO_34$.[25-27] Herein, the structural properties of $(1\text{-}x)BaTiO_3$–$xBiScO_3$ and $(1\text{-}x)PbTiO_3$–$xBiScO_3$ is discussed through the analysis of XANES data and supporting XRD data. The effect $BiScO_3$ substitution has on the local structure of $BaTiO_3$ and $PbTiO_3$ has not been extensively investigated, particularly with

respect to the *B*-site cations (i.e.Ti^{4+} and Sc^{3+}). The effect of a change in composition on the oxidation state of Bi was also investigated by studying Bi L_3-edge XANES spectra.

2. Experimental

2.1. Synthesis

All reagents ($PbCO_3$, Bi_2O_3, $BaCO_3$, TiO_2, Sc_2O_3) were obtained from Sigma-Aldrich or Aithaca with purities better than 99 %. The (1-*x*)$BaTiO_3$–*x*$BiScO_3$ ($0 \leq x \leq 0.4$ in 0.1 increments) and (1-*x*)$PbTiO_3$–*x*$BiScO_3$, ($0 \leq x \leq 0.3$ in 0.1 increments) samples were prepared by finely mixing stoichiometric amounts of each reagent under acetone with a mortar and pestle. The powders were then pressed into pellets, heated to 800 ^oC for 4 h, and quench cooled in air. Samples were reground, pressed, and heated to 1200 ^oC for 24 h. This process was repeated until single phase samples were observed by powder X-ray diffraction (XRD). Attempts to prepare pure-phase samples of (1-*x*)$BaTiO_3$–*x*$BiScO_3$ and (1-*x*)$PbTiO_3$–*x*$BiScO_3$ with $x \geq 0.5$ and $x \geq 0.4$, respectively, were hampered by the presence of impurity phases (i.e. Bi_2O_3 and $Bi_{20}TiO_{32}$).

2.2. Powder X-ray Diffraction

Structural determination of (1-*x*)$BaTiO_3$–*x*$BiScO_3$ and (1-*x*)$PbTiO_3$–*x*$BiScO_3$ was performed using powder XRD. Powder diffraction patterns were collected using a PANalytical Empyrean X-ray diffractometer equipped with a Co $K\alpha_{1,2}$ X-ray source (1.789 Å) over an angular range of $10^o \leq 2\theta \leq 80^o$. Samples were ground into a fine powder and mounted on glass slides using ethanol before being placed on a spinning stage to prevent preferred orientation effects. Rietveld refinements were performed on the diffraction patterns using the PANalytical X'pert HighScore Plus software program.[30] Initial structural models were adapted from the previously reported structures of both perovskite solid solutions.[10,22] Peak shapes were modelled using a pseudo-Voigt function and the background was fitted using a third-order polynomial function. Structural and profile parameters were varied during the refinement.

106 **2.3. XANES Analysis**

107 The Sc and Ti K-edge XANES spectra were collected using the Canadian Light
108 Source/X-ray Science Division Collaborative Access Team (CLS@APS, Sector 20) bending
109 magnetic beamline (20BM) located at the Advanced Photon Source (APS), Argonne National
110 Laboratory.[31] Finely ground samples were sandwiched between Kapton tape and positioned
111 45° to the X-ray beam. The thickness of the samples was varied by adding or removing layers
112 to maximize the absorption-edge jump. A Si (111) double crystal monochromator with
113 harmonic rejection provided a flux of ~10^{11} photons/sec. An X-ray beam size of 1 x 3 mm was
114 used with the spectral resolution being 0.7 eV at 4966 eV (Ti K-edge).[32] The spectra were
115 recorded in transmission mode using ionization chambers filled with 80% helium and 20%
116 nitrogen to achieve optimal absorption-edge step heights and signal-to-noise ratios. Metal
117 standards were placed behind the sample and measured concurrently in transmission mode.
118 The Sc K-edge spectra were calibrated using Sc foil with the lowest energy peak maximum in
119 the first derivative of the Sc metal K-edge spectrum set to 4492 eV.[32] The Ti K-edge spectra
120 were calibrated using Ti foil with the lowest energy peak maximum in the first derivative of
121 the Ti metal K-edge spectrum set to 4966 eV.[32]

122 The Bi L_3-edge XANES spectra were collected using the Very Sensitive Elemental and
123 Structural Probe Employing Radiation from a Synchrotron (VESPERS; 07B2-1) beamline
124 located at the Canadian Light Source (Saskatoon, Canada).[33] Samples were prepared by
125 dusting a single layer of finely ground sample onto Kapton tape. Samples were mounted
126 perpendicular to the beamline at an angle of 45°. Monochromatic X-rays were obtained using
127 a Si(111) monochromator that provided a flux of ~10^{10} photons/sec. An X-ray beam size of
128 0.8 x 0.8 mm^2 was used and spectra were collected in fluorescence mode using a 4-element
129 silicon drift Vortex detector. An energy step-size of 0.2 eV was used through the absorption
130 edge. Spectra were calibrated against Pb metal foil with the maximum in the first derivative

of the Pb metal L_3-edge set to 13035 eV.[32] Note that the Bi L_3-edge XANES spectra were not corrected for self-absorption. Given the small amount of Bi in these materials, it is unlikely that self-absorption effects will have a significant impact on the lineshape of the Bi L-edge spectra. All XANES spectra reported herein were analyzed using the Athena software package.[32]

3. Results and Discussion

3.1. Diffraction analysis

The fitted XRD patterns from (1-*x*)$BaTiO_3$–*x*$BiScO_3$ ($x \leq 0.4$) and (1-*x*)$PbTiO_3$–*x*$BiScO_3$ ($x \leq 0.3$) are shown in Figure 2. The Rietveld refinement results are summarized in Table 1. The lattice parameters from (1-*x*)$BaTiO_3$–*x*$BiScO_3$ and (1-*x*)$PbTiO_3$–*x*$BiScO_3$ were plotted as a function of *x* and are shown in Figure 3. Substituting $BiScO_3$ into $BaTiO_3$ or $PbTiO_3$ results in an overall increase in the unit cell volume. For the tetragonal *P4mm* phases, $BiScO_3$-substitution results in a decrease in the *a* parameter and an increase in the *c* parameter. This is also evident by the merging of the (002) and (020) reflections in the XRD patterns (see Figure 4). A larger increase in the overall displacement parameter was observed in the (1-*x*)$BaTiO_3$–*x*$BiScO_3$ solid solution, suggesting that $BiScO_3$ substitution in $BaTiO_3$ results in an overall larger degree of structural disorder. The solid solution range of (1-*x*)$BaTiO_3$–x$BiScO_3$ is consistent with previous studies[21,22] while the solid solution range of the (1-*x*)$PbTiO_3$–*x*$BiScO_3$ is lower than previously reported, which is likely due to differences in reaction conditions.[10] All samples in the (1-x)$PbTiO_3$–*x*$BiScO_3$ solid solution were fitted to the tetragonal *P4mm* perovskite phase. Members of the (1-x)$BaTiO_3$–*x*$BiScO_3$ solid solution were fitted to the tetragonal *P4mm* perovskite phase at $x < 0.2$ and the cubic *$Pm\bar{3}m$ phase at $x > 0.2$*. At $x = 0.2$, refinement of theXRD pattern indicated that there were two phases present consisting of tetragonal *P4mm* phase and either the cubic *$Pm\bar{3}m$* or rhombohedral *R3m* phase. Similar goodness of fit (χ^2) were obtained when fitting the pattern to both two-phase models.

Previous diffraction studies have noted the presence of a similar two-phase region near this composition, consisting of a tetragonal *P4mm* phase and a rhombohedral *R3m* phase exhibiting pseudo-cubic symmetry.[22] It is likely that the rhombohedral *R3m* phase is similar in structure to the cubic $Pm\bar{3}m$ phase and cannot be distinguished via laboratory XRD. Regardless, substituting $BiScO_3$ into $BaTiO_3$ results in the formation of a cubic-like perovskite structure. Also, the *A*-and *B*-site occupancy parameters were refined to allow for cation-site disorder. Refining the occupancy parameters resulted in no observable improvement in the χ^2 value of most diffraction patterns, suggesting that there was no cation site disorder. The χ^2 value for the fitted pattern of $0.6BaTiO_3$–$0.4BiScO_3$ was slightly improved when refining the site occupancy parameters, decreasing from 2.09 to 1.99. Refinement of the occupancy parameters suggested that Bi and Sc may occupy 3.8 % of the *B*- and *A*-site, respectively.

Note that the characteristic superlattice reflections associated with the tetragonal *P4mm* phase (i.e. the (002) and (020) reflections) disappears at $x = 0.1$, suggesting a phase transformation occurs at this composition. Attempts were made to fit the pattern to a two-phase model consisting of the *P4mm* phase and either the cubic $Pm\bar{3}m$ or rhombohedal *R3m* phases. Fitting the pattern to the P4mm + $Pm\bar{3}m$ model indicated that this composition consistent of mostly of the *P4mm* phase (98.6%). Refinements that included the *R3m* and *P4mm* phases would fit the pattern to only the *P4mm* phase. This indicates that the tetragonal *P4mm* structure is the predominant perovskite phase at $x = 0.1$.

In general, the phases observed in the $(1-x)BaTiO_3$–$xBiScO_3$ and $(1-x)PbTiO_3$–$xBiScO_3$ solid solutions conforms to the Goldschmidt's tolerance factor (*t*), an empirical tool used to predict the stability and distortions in perovskites.[34] The tolerance factor is defined as:

$$t = \frac{r_A + r_O}{\sqrt{2}(r_B + r_{O)}} \qquad (1)$$

where r_A is the ionic radius of the 12-cooridinate *A*-site cation, r_B the ionic radius of the 6-coordinate *B*-site cation, and r_O the ionic radius of 6-coordinate O^{2-} anion. Perovskites phases

are expected to form when t falls between 0.88–1.09, assuming Shannon's ionic radii rules.[35,36] Cubic perovskites are expected to form at $t = 1$. Perovskites with $t > 1$ typically form tetragonal phases and perovskites with $t < 1$ favours the formation of low symmetry phases such as rhombohedral, orthorhombic, or monoclinic structures. $BaTiO_3$ and $PbTiO_3$ have tolerance factors of 1.06 and 1.02, respectively, consistent with the formation of the tetragonal *P4mm* perovskite structure. Substituting $BiScO_3$ into $BaTiO_3$ and $PbTiO_3$ lowers the tolerance factor and should result in an overall decrease in tetragonal structural distortions. The XRD results reported here generally agrees with this prediction as the cubic $Pm\bar{3}m$ phase forms in $0.8BaTiO_3$–$0.2BiScO_3$ where $t = 1.01$.

Information on Ti^{4+}/Sc^{3+} off-centre displacement in each solid solution can be obtained from the Ti^{4+}/Sc^{3+} atomic coordinates (½, ½, z), particularly the z parameter (see Table 1). The z parameter correlates with the displacement of the Ti^{4+}/Sc^{3+} cations along the z-direction in the *P4mm* phase. In general, Ti^{4+}/Sc^{3+} displacement increases as the z_{1b} parameter deviates from 0.5. The Ti^{4+}/Sc^{3+} z parameters for (1-x)$BaTiO_3$–$x$$BiScO_3$ and (1-x)$PbTiO_3$–$x$$BiScO_3$ are listed in Table 1. The Ti^{4+}/Sc^{3+} z_{1b} parameter in the (1-x)$BaTiO_3$–$x$$BiScO_3$ solid solution approaches 0.5 with increasing x, suggesting that Ti^{4+}/Sc^{3+} displacement decreases until the cubic $Pm\bar{3}m$ phase forms.

3.2. XANES analysis

3.2.1. Ti K-edge XANES

The Ti K-edge XANES spectra from representative members of the (1-x)$BaTiO_3$–$x$$BiScO_3$ and (1-x)$PbTiO_3$–$x$$BiScO_3$ solid solutions are shown in Figure 5. The Ti K-edge XANES spectra consists of two major regions: the main edge (Region A) and the pre-edge (Region B).[37] The main edge corresponds to a dipole-allowed transition of Ti 1s electrons into unoccupied 4p states and is highly dependent on the oxidation state (i.e., absorption edge energy) and local coordination environment of Ti (i.e., lineshape).[38,39] $BiScO_3$ substitution has

no effect on the Ti K-edge absorption edge energy of $PbTiO_3$ and $BaTiO_3$, indicating that Ti remains tetravalent in both solid solutions. Differences in the lineshape between $BaTiO_3$ and $PbTiO_3$–based solid solutions is likely due to differences in the hybridization of Ti 4p states with the nearest and next-nearest neighbours bonding states (i.e., Ba 6p vs Pb 6p). The intensity of the main edge features of $BaTiO_3$ becomes broader with $BiScO_3$ substitution. The lineshape of the Ti K-edge main edge feature is known to be sensitive to local disorder around the absorbing Ti atom.[39-42] Local disorder around the absorbing atom generally results in greater destructive interference in the multiple scattering contributions to the main edge. This leads to the broadening of features in main edge region of the Ti K-edge.[39,40] Peak broadening observed in the Ti K-edge XANES spectra of $(1\text{-}x)BaTiO_3$–$xBiScO_3$ is likely due to increased structural disorder. Note that similar broadening was not observed in the Ti K-edge of $(1\text{-}x)PbTiO_3$–$xBiScO_3$ (see Figure 5b), suggesting that there is little local disorder.

The Ti K-edge pre-edge corresponds to the dipole-forbidden transition of 1s electrons into unoccupied 3d states. The probability of a dipole forbidden transition is low compared to a dipole-allowed transition. As such, features in the pre-edge will be significantly less intense than those observed in the main edge. The pre-edge features can be enhanced through overlap of the d states with p states of the adsorbing atom and neighbouring atoms.[37] Therefore, the pre-edge will be influenced by both the oxidation state (i.e., number of available d states) and the coordination environment of the absorbing atoms (i.e., p-d mixing).[37] Analysis of the main-edge features suggested that $BiScO_3$ substitutions does not change the oxidation state of Ti^{4+}. As such, any changes in the pre-edge induced by $BiScO_3$ substitution will likely be due to changes in the local coordination environment of Ti^{4+} cations. There are four major features observed in the Ti K-edge pre-edge. In titanium-based perovskite systems, feature B1 and B2 corresponds to the transition of a 1s electron into unoccupied t_{2g} and e_g^* states, respectively.[43-52] Feature B2 is generally more intense than B1 due to a strong degree of hybridization between

231 Ti e_g^* states with Ti 4p and neighbouring O 2p states.[46] For (1-x)$BaTiO_3$–$xBiScO_3$, feature B2
232 increases in intensity with x, indicating an increase in p-d overlap. Several studies have shown
233 that this feature is sensitive to the off-centre displacement of Ti^{4+} cations due to small changes
234 in the p-d overlap.[25,43,46,47, 50-52] The intensity of feature B2 is related to the off-centre
235 displacement of Ti^{4+} by the following equation: [25,50-52]

236 $$I_{B2} = \frac{\delta_{Ti}^2}{a_O^{5.5}}$$

237 where I_{B2} is the intensity of feature B2, δ_{Ti}^2 is the off-centre displacement of Ti^{4+} cations, and
238 a_o is the size of the TiO_6 octahedron. Therefore, the intensity of feature B2 is directly
239 proportional to the mean-squared off-centre displacement of the Ti^{4+} cation.[25] The increase in
240 feature B2 is likely due to an increase in Ti^{4+} off-centre displacement with $BiScO_3$
241 substitution.[26] Note that the pre-edge feature is only proportional to the magnitude of the off-
242 centre displacement of Ti^{4+} cations and not the direction. It is possible that $BiScO_3$-substituion
243 can change the direction of the displacement of Ti^{4+} cations. However, this cannot be inferred
244 from the Ti K-edge pre-edge. Also, no observable changes in the intensity of B2 were observed
245 in (1-x)$PbTiO_3$–$xBiScO_3$, suggesting that $BiScO_3$ has no effect on the displacement of Ti^{4+}
246 cations.

247 Features B3 and B4 are similar to those observed in other Ti-based perovskite
248 systems.[26,27,50] These features could only be reproduced in model spectra constructed from a
249 large (greater than 50) cluster of atoms, suggesting that these transitions originate from the
250 transition of the 1s electron into next-nearest neighbour d states.[50] Feature B3 corresponds to
251 the transition of a Ti 1s electron into the neighbouring Ti atoms 3d states.[25,26,50] The intensity
252 of feature B3 decreases with x in (1-x)$BaTiO_3$–$xBiScO_3$ and is consistent with a decrease in the
253 number of neighouring Ti 3d states. Feature B4 is similar to a feature observed in $BaTi_{1-x}Zr_xO_3$
254 and $(Bi_{0.5}Na_{0.5})Ti_{1-x}Zr_xO_3$ that is assigned to the transition of a Ti 1s electrons into neighouring
255 Zr 4d states. [25,26,50] Given the relative size different between Ti^{4+} (0.61 Å) and Sc^{3+} (0.745 Å)

cations,[35] it is likely that Sc^{3+} would have a larger crystal field splitting energy than Ti^{4+}. Therefore, feature B4 could be assigned to the transition of a Ti 1s electron into neighbouring Sc 3d states. The increase in the intensity of B4 with x in (1-x)$BaTiO_3$–$xBiScO_3$ suggests that there is an increase in the number of neighbouring Sc^{3+} cations. Overall, trends in features B3 and B4 suggests that there is no local clustering of Ti^{4+} cations throughout the (1-x)$BaTiO_3$–$xBiScO_3$ system. Note that there are relatively little changes in the intensity of features B3 and B4 in (1-x)$PbTiO_3$–$xBiScO_3$, suggesting that $BiScO_3$ substitution has little effect on Ti^{4+} off-centre displacement.

3.2.2. Sc K-edge XANES

Compared to the other transition metals, there is relatively little work reported on the Sc K-edge XANES spectra.[53-56] As shown in Figure 6, the Sc K-edge lineshape is similar to that of Ti, consisting of two major regions representing the main edge (Sc 1s-to-Sc 4p transition: Region A) and the pre-edge (Sc 1s-to-Sc 3d transition; Region B). Three features (labelled B1-B3) are observed in the Sc K-edge pre-edge region that are similar to the features observed in the Ti K-edge pre-edge region. Previous studies of the Sc K-edge pre-edge features have demonstrated that the intensity of the pre-edge is sensitive to the local coordination environment of Sc^{3+} cations.[53] Features B1 and B2 corresponds to the transition of a Sc 1s electron in Sc t_{2g} and e_g^* states, respectively. Feature B2 should be sensitive to the displacement of Sc^{3+} cations due to the overlap of Sc 3d e_g^* and O 2p states. In both solid solutions, the intensity of B2 does not change with x, indicating that substitution appears to have little to no effect on the displacement of Sc^{3+} cations. Feature B3 likely corresponds to the transition of a Sc 1s electron into neighbouring Sc 3d states. Like other features in the pre-edge, there is no change in the intensity of this feature in either solid solution, suggesting that there is no change in the number of neighbouring Sc^{3+} cations. Surprisingly, the main edge broadens with increasing x, which is consistent with increased structural distortion. There were no lineshape

changes observed in the Sc K-edge XANES spectra from (1-x)$PbTiO_3$–$x$$BiScO_3$, suggesting that there is little local disorder of the Sc^{3+} local environment.

3.2.3. Bi L_3-edge XANES

Broadening of the Ti K-edge XANES spectra of (1-x)$BaTiO_3$–$x$$BiScO_3$ suggests that $BiScO_3$ substitution increases local disorder. XRD analysis also indicated that there may be a small degree of cation site disorder may occur in the (1-x)$BaTiO_3$–$x$$BiScO_3$ solid solution. However, the ionic radius of Bi^{3+} (1.17 Å) is likely too large to substitute into the *B*-site. However, Bi can occupy the *B*-site in an ABO_3 perovskite in the form of Bi^{4+}, which disporportionates into Bi^{3+} and Bi^{5+}.[57] If metal site disorder occurs in (1-x)$BaTiO_3$–$x$$BiScO_3$, the oxidation state of Bi should increase with x due to the presence of Bi^{5+}. As such, the oxidation state of (1-x)$BaTiO_3$–$x$$BiScO_3$ and (1-x)$PbTiO_3$–$x$$BiScO_3$ was investigated by analyzing the Bi L_3-edge XANES spectra (see Figure 7). The lineshape of the Bi L_3-edge is influenced by both the Bi oxidation state and local structure.[58,59] This is evident when comparing the Bi L_3-edge spectra for Bi_2O_3 (Bi^{3+}) and $Ba_{1.5}Sr_{0.5}BiLuO_6$ (Bi^{5+}). The Bi L_3-edge of $Ba_{1.5}Sr_{0.5}BiLuO_6$ consists of three well-defined features (labelled A-C) compared to the two broad peaks (labelled A and B) observed in Bi_2O_3. The features in the Bi L_3-edge XANES spectrum from Bi_2O_3 corresponds to a dipole-allowed transition of Bi 2p electrons into unoccupied Bi 5d states, which split into bonding (Feature A) and anti-bonding (Feature B) Bi 5d states.[59] These features are shifted to higher energies in $Ba_{1.5}Sr_{0.5}LuBiO_6$ due to the higher oxidation state of Bi. An additional low energy feature (Feature C) is observed in the spectrum from $Ba_{1.5}Sr_{0.5}LuBiO_6$ that corresponds to a dipole-allowed transition of Bi 2p electrons into unoccupied Bi 6s states.[59] The Bi L_3-edge lineshape and absorption edge energies of (1-x)$BaTiO_3$-$x$$BiScO_3$ and (1-x)$PbTiO_3$-$x$$BiScO_3$ are similar to that of Bi_2O_3, consistent with the presence of Bi^{3+} in both solid solutions. The observation of no apparent lineshapes changes in

either solid solution indicates that Bi remains trivalent. Therefore, it is unlikely that Bi cations occupy the *B*-site in either perovskite solid solution.

4. Conclusion

The long-range and local structures of (1-*x*)$BaTiO_3$–*x*$BiScO_3$ and (1-*x*)$PbTiO_3$–*x*$BiScO_3$ were investigated using XANES. Refinement of the X-ray diffraction patterns showed that (1-*x*)$BaTiO_3$–*x*$BiScO_3$ undergoes a tetragonal (*P4mm*) to cubic ($Pm\bar{3}m$) phase transformation at $x = 0.2$. XANES analysis showed that substituting $BiScO_3$ into $BaTiO_3$ increases the off-centre displacement of Ti^{4+} cations but has little effect on the off-centre displacement of Sc^{3+} cations. XANES analysis also showed that $BiScO_3$ substitution into $PbTiO_3$ has little effect on the local structure of the Ti^{4+} and Sc^{3+} cations despite (1-*x*)$PbTiO_3$–*x*$BiScO_3$ showing enhanced ferroelectric behaviour at a MPB.[10] This is likely due to the influence of the Pb^{2+} and Bi^{3+} $6s^2$ lone pairs. Ordering of the Pb^{2+} $6s^2$ lone pair in $PbTiO_3$ displaces Pb^{2+} cation from the centre of the *A*-site, which also induces additional displacement of the Ti^{4+} cation.[18] Introducing another lone pair active cation (i.e. Bi^{3+}) into the *A*-site of $PbTiO_3$ may not result in additional Ti^{4+} cation displacement due to the existing lone pair active cation (i.e. Pb^{2+}). Substituting Bi^{3+} into the *A*-site of $BaTiO_3$ enhance the off-centre displacement of Ti^{4+} cations as $BaTiO_3$ does not contain a lone pair active cation. Studies on the local structure of Bi^{3+} cations in (1-*x*)$BaTiO_3$–*x*$BiScO_3$.showed that Bi^{3+} cations are displaced from their ideal position, suggesting that the $6s^2$ lone pairs are ordered.[28] Note that the influence of the Bi^{3+} $6s^2$ lone pair on the off-centre displacement of the Sc^{3+} cations may also explain by the local structure of Sc^{3+} cations are relatively insensitive to substitution. Overall, this study suggests that the *A*-site cation has a noticeable effect on the local structure of the *B*-site cation in perovskite materials.

Finally, it is interesting to note that $BiScO_3$ substitution in $BaTiO_3$ does not result in enhanced ferroelectric behaviour despite an increase in Ti^{4+} off-centre displacement. This may

be due to an increase in local disorder observed in the Ti and Sc K-edge of (1-*x*)$BaTiO_3$–*x*$BiScO_3$. Increased local disorder may favor relaxor ferroelectric behaviour rather than normal ferroelectric behaviour.[22,23]

5. Acknowledgments

The Natural Sciences and Engineering Research Council (NSERC) of Canada supported this work through a discovery grant awarded to A.P.G. The Canadian Foundation for Innovation (CFI) is thanked for providing funds to purchase the PANalytical Empyrean powder X-ray diffractometer used in this work. The authors extend their thanks to Dr. Zou Finfrock for help in carrying out XAS measurements at 20BM (CLS@APS Sector 20, APS) and Dr. Renfei Feng for help in carrying out XAS measurements at the VESPERS beamline (07B2-1, CLS). In addition, Dr. M. R. Raffiudin and Dr. J. Hayes (Department of Chemistry, University of Saskatchewan) are thanked for helping with the collection of the XANES spectra presented in this study. Access to Sector 20 was obtained through the CLS-APS Partnership Agreement. Sector 20 facilities at the Advanced Photon Source and research at these facilities are supported by the U.S. Department of Energy-Basic Energy Sciences, the Canadian Light Source and its funding partners, the University of Washington, and the Advanced Photon Source. Use of the Advanced Photon Source, an Office of Science User Facility operated for the U.S. Department of Energy (DOE) Office of Science by Argonne National Laboratory, was supported by the U.S. DOE under Contract No. DE-AC02-06CH11357. The CLS is supported by NSERC, the National Research Council of Canada, the Canadian Institutes of Health Research, the Province of Saskatchewan, Western Economic Diversification Canada, and the University of Saskatchewan.

6. References

1. G. H. Haertling, Ferroelectric Ceramics: History and Technology. *J. Am. Ceram. Soc.* (1999) **82**, 797-818.

2. D. Fiore, R.L. Gentilman, H. Pham-Nguyen, W.J. Serwatka, P.T. McGuire, C.D. Near, L.J. Bowen 1-3 piezocomposite SmartPanels. *Proc. SPIE* (1997) **3044**, 391-396.

3. N. Izyumskaya, Y. I. Alivov, S. J. Cho, H. Morkoç, H. Lee, Y. S. Kang, Processing, structure, properties, and applications of PZT thin films. *Crit. Rev. Solid State Mater. Sci.* (2007) **32**, 111-202.

4. M. T. Ghoneim, M. A. Zidan, M. Y. Alnassar, A. N. Hanna, J. Kosel, K. N. Salama, M. M. Hussain, Thin PZT_based ferroelectric capacitors on flexible silicon for nonvolatile memory applications. *Adv. Electron. Mater.* (2015) **1**, 1500045.

5. B. Jaffe, W. R. Cook, H. Jaffe, Piezoelectric Ceramics (Academic, London, 1971).

6. S. L.Swartz, Topics in electronic ceramics. *IEEE Trans. Electr. Insul.* (1990) **25**, 933-987.

7. E. Ringgaard, T. Wurlitzer, Lead-free piezoceramics based on alkali niobates *J. Eur. Ceram. Soc.* (2005) **25**, 2701-2706.

8. P. K. Panda, Environmental friendly lead-free piezoelectric materials. *J. Mater. Sci.* (2009) **44**, 5049-5062.

9. R.E. Cohen, Origin of ferroelectricity in perovskite oxides. *Nature* (1992) **358** 136-138.

10. R.E. Eitel, C.A. Randall, T.R. Shrout, S.E. Park, Preparation and characterization of high temperature perovskite ferroelectrics in the solid solution (1-x)$BiScO_3$–$x$$PbTiO_3$. *Jpn. J. Appl. Phys.* (2002) **41** 2099-2104.

11. K.X. Sun, S.Y. Zhang, K. Wasa, X.J. Shui, Optimized properties of $x$$BiInO_3$–(1-$x$)$PbTiO_3$ thin films deposited by an RF-magnetron sputtering method. *Phys. Status Solidi* (2016) **213**, 2479-2484.

12. G. Feng, H. Rongzi, L. Jiaji, L. Zhen, C. Lihong, T. Changsheng, Phase formation and characterization of high Curie temperature xBiYbO$_3$–(1-x)PbTiO$_3$ piezoelectric ceramics. *J. Euro. Ceram. Soc.* (2009) **29**, 1687-1693.

13. J. Cheng, W. Zhu, N. Li, L.E. Cross, Fabrication and characterization of xBiGaO$_3$–(1-x)PbTiO$_3$: A high temperature reduced Pb-content piezoelectric ceramic. *Mater. Lett.*. (2003) **57**, 2090-2094.

14. J. Iniguez, D. Vanderbilt, L. Bellaiche, First-principles study of (BiScO$_3$)$_{1-x}$–(PbTiO$_3$)$_x$ piezoelectric alloys. *Phys. Rev. B* (2003) **67**, 224107.

15. R.E. Eitel, C.A. Randall, T.R. Shrout, P.W. Rehrig, W. Hackenberger, S.E. Park, New high temperature morphotropic phase boundary piezoelectrics based on (Bi(Me)O$_3$–PbTiO$_3$ ceramics. *Jpn. Appl. Phys.* (2001) **40**, 5999-6002.

16. K.V. Lalitha, A. N. Finch, R. Ranjan, Correlations between enhanced lattice polarizability and high piezoelectric response in BiScO$_3$–PbTiO$_3$. *Phys. Rev. B* (2013) **87**, 064106.

17. Y. Shimojo, A. Miyaguchi, M. Yoshida, T. Katsumata, Y. Shimojo, R. Wang, T. Sekiya, High-pressure synthesis and ferroelectric properties in perovskite-type BiScO$_3$-PbTiO$_3$ solid solution. *J. Appl. Phys.* (2004) **95**, 231-235.

18. K M. Kabe, C.H. Ahn, J. M. Triscone Physics of Ferroelectrics, A Modern Perspective (2007) Berlin: Springer.

19. A.A. Belik, S. Iikubo, K. Kodama, N. Igawa, S.I Shamoto, M. Maie, T. Nagai, Y. Matsui, S. Yu, S. Bogdan, B.I. Lazoryak, E. Takaayama-Muromachi, BiScO$_3$: Centrosymmetric BiMnO$_3$-type oxide. *J. Am. Chem. Soc.* (2006) **126,** 706-707.

20. V. Polinger, P. Garcia-Fernandez, I'B' Bersuker, Pseudo Jahn-Teller origin of ferroelectric instability in BaTiO$_3$ type perovskites: The Green's function approach and beyond. *Physica B* (2015) **457**, 296-309.

403 21. H. Ogihara, C.A. Randall, S. Trolier-McKinstry, Weakly coupled relaxor behaviour of
404 $BaTiO_3$–$BiScO_3$ ceramics. *J. Am. Ceram. Soc.* (2009) **92**, 110-118.
405 22. K. Datta, P.A. Thomas, Structural investigation of a novel perovskite-based lead-free
406 ceramics: $x$$BiScO_3$–(1-$x$)$BaTiO_3$ *J. Appl. Phys.* (2010) **107**, 043516.
407 23. K. Band, M.V. Takarkhede, A Transition from relaxor to normal ferroelectric: An
408 overview. *Int. J. Eng. Res. Tech.* (2013) **2**, 635-638.
409 24. Z. Yao, H. Liu, Y. Liu, Z. Li, X. Cheng, M. Cao, H. Hao, *J. Ceram. Soc. Jpn.* (2008)
410 **116**, 1150-1153.
411 25. I. Levin, E. Cockayne, V. Krayzman, J.C. Woicik, S. Lee, C.A. Randall, Local structure
412 of Ba(Ti,Zr)O_3 perovskite-like solid solutions and its relation to the band-gap behavior *Phys.*
413 *Rev. B* (2011) **83**, 094122.
414 26. P.E.R. Blanchard, S. Liu, B.J. Kennedy, C.D. Ling, Z. Zhang, M. Avdeev, L.Y. Jang,
415 J.F. Lee, C.W. Pao, J.L. Chen, Studying the effects of Zr-doping in $(Bi_{0.5}Na_{0.5})TiO_3$ via
416 diffraction and spectroscopy *Dalton Trans.* (2014) **43**, 17358-17365.
417 27. S. Liu, P.E.R. Blanchard, B.J. Kennedy, Z. Zhang, C.D. Ling, Long- and short-range studies
418 of KBT-KBZ solid-solutions using synchrotron radiation. *Dalton Trans.* (2015) **44**, 10681-
419 10688.
420 28. I. Levin, V. Krayzman, J.C. Woicik, F. Bridges, G. E. Sterbinsky, T.M. Usher, J.L.
421 Jones, D. Torrejon, Local Structure of $BaTiO_3$–$BiScO_3$ dipole glasses *Phys. Rev. B* (2016) *93*,
422 104106.
423 29. V. Krayzman, I. Levin, J.C. Woicik, Ti K-XANES analysis of the cation distribution
424 in the $CaTi_{1-x}Zr_xO_3$ solid solution. *AIP Conf. Proc.* (2007) **882**, 434-435..
425 30. PANalytical B.V., X'Pert HighScore Plus, version 3.0, Almelo, The Netherlands, 2011.

31. S.M. Heald, D.L. Brewe, E.A. Stern, K.H. Kim, F.C. Brown, D.T. Jiang, E.D. Crozier, R.A. Gordon, XAFS and micro-XAFS at the PNC-CAT beamlines *J. Synchrotron Rad.* (1999) **6**, 347-349.

32. B. Ravel, M. Newville, ATHENA, ARTEMIS, HEPHAESTUS: data analysis for X-ray absorption spectroscopy using IFEFFIT. *J. Synchrotron Rad.* (2005) **12**, 537-541

33. R. Feng, A. Gerson, G. Ice, R. Reininger, B. Yates, S. McIntyre, VESPERS: a beamline for combined XRF and XRD measurements *AIP Conf. Proc.* (2007) **879**, 872-874.

34. V.M. Goldschmidt, Die Gesetze der Krystallochemie *Naturwissenschaften* (1926) **14**, 477–485.

35. R.D. Shannon, Revised effective ionic radii and systematic studies of interatomic distances in halides and chalcogenides, *Acta. Cryst.* (1976) **A32**, 751-767.

36. M.R. Suchomel, P.K. Davies, Predicting the position of the morphotropic phase boundary in high temperature $PbTiO_3$–$Bi(B'B'')O_3$ based dielectric ceramics. *J. Appl. Phys.* (2005) **96**, 4405-4410.

37. T. Yamamoto, Assignment of pre-edge peaks in K-edge X-ray absorption spectra of 3d transition metal compounds: electric dipole or quadrupole. *X-ray Spectrom.* (2008) **37**, 572-584.

38. E.R. Aluri, A.P. Grosvenor, A study of the electron structure and structural stability of $Gd_2Ti_2O_7$ based glass-ceramic composites. *RSC Adv.* (2015) **5** 80939-80949.

39. F. Farges, G.E. Brown Jr., J.J. Rehr, Ti K-edge XANES studies of Ti coordination and disorder in oxide compounds: Comparison between theory and experiment. *Phys. Rev. B* (1997) **56**, 1809-1819.

40. F. Farges, G.E. Brown Jr., J.J. Rehr, Coordination chemistry of Ti(IV) in silicate glasses and melts: I. XAFS study of titanium coordination in oxide model compounds. *Geochim. Cosmochim. Acta* (1996) **60**, 3023-3038.

451 41. A.L. Ankudinov, J.J. Rehr, S.D. Conradson, Real-space multiple-scattering calculation
452 and interpretation of X-ray absorption near-edge structure. *Phys. Rev. B* (1998) **58**, 7565-7576.
453 42. Z. Zhang, M. Avdeev, M. de los Reyes, G.R. Lumpkin, B.J. Kennedy, P.E.R.
454 Blanchard, S. Liu, A. Tadich, B.C.C Cowie, Probing long- and short-range disorder in $Y_2Ti_{2-x}Hf_xO_7$ by diffraction and spectroscopy techniques, *J. Phys. Chem. C* (2016) **120**, 26465-26479.
456 43. P. Jaiban, S. Buntham, A. Watcharapasorn, Dielectric properties of (1-
457 x)$Sr_{0.92}La_{0.08}TiO_3$–(x)$LaMn_{0.98}Nb_{0.02}O_3$ ceramics under violet light irradiation. *Mater. Lett.*
458 (2017) **193**, 133-137.
459 44. P. Jaiban, A. Watcharapasorn, R. Yimnirun, R. Guo, A. S. Bhalla, Effects of donor and
460 acceptor doping on dielectric and ferroelectric properties of $Ba_{0.7}Ca_{0.3}TiO_3$ lead-free ceramics
461 *J. Alloys Compd.* (2017) **695**, 1329-1335.
462 45. A. Yoshiasa, T. Nakatani, T. Hiratoko, T. Tobase, A. Nakatsuka, M. Okube, H. Arima,
463 K. Sugiyama, Temperature dependence of Zr and Ti K-edge XANES spectra for para- and
464 ferro-electric perovskite-type $PbZrO_3$, $PbTiO_3$, and $BaTiO_3$ *J. Phys. Conf. Ser.* (2016) **712**,
465 012121.
466 46. N. Jiang, D. Su, J.C.H. Spence, Determination of Ti coordination from pre-edge peaks
467 in Ti K-edge XANES *Phys. Rev. B* (2007) **76**, 214117.
468 47. A. Bootchanont, J. Jutimoosik, S. Chandarak, M. Unruan, P. Kidkhunthod, W.
469 Klysubun, S. Rujirawat, R. Yimnirun, R. Guo, A. Bhalla, Synchrotron X-ray absorption
470 spectroscopy study of local structure transformation behavior in perovskite $Ba(Ti,Zr)O_3$
471 system *J. Alloys Compd.* (2014) **616**, 430-435.
472 48. D. Cabaret, A. Bordage, A. Juhin, M. Arfaoui, E. Gaudry, First-principles calculations
473 of X-ray absorption spectra at the K-edge of 3d transition metals: an electronic structure
474 analysis of the pre-edge *Phys. Chem. Chem. Phys.* (2010) **12**, 5619-5633.

475 49. D. Cabaret, Y. Joly, H. Renevier, C. R. Natoli, Pre-edge structure analysis of Ti K-edge
476 polarized X-ray absorption spectra in TiO_2 by full-potential XANES calculations *J.*
477 *Synchrotron Rad.* (1999) **6**, 258-260.
478 50. R.V. Vedrinskii, V.L. Kraizman, A.A. Novakovich, Ph.V. Demekhin, S.V. Urazhdin,
479 Pre-edge fine structure of the 3d atom K X-ray absorption spectra and quantitative atomic
480 structure determinations for ferroelectric perovskite structure crystals. *J. Phys.: Condens.*
481 *Matter* (1998) **10**, 9561-9580.
482 51. A.I. Frenkel, Y. Feldman, V. Lyahovitskaya, E. Wachtel, I. Lubomirsky Microscopic
483 origin of polarity in quasiamorphous $BaTiO_3$ *Phys. Rev. B* (2005) **71**, 024116.
484 52. B. Ravel, E.A. Stern, R.I. Vedrinskii, V. Kraizman Local structure and the phase
485 transition of $BaTiO_3$ *Ferroelectr.* (1998) **206-207**, 407-410.
486 53. P. Lindqvist-Reis, I. Persson, M. Sandstrom The hydration of the scandium (III) ion in
487 aqueous solution and crystalline hydrates studied by XAFS spectroscopy, large-angle X-ray
488 scattering and crystallography *Dalton Trans.* (2006) **32**, 3868-3878.
489 54. J.R. Hayes, A.P. Grosvenor, Investigation of the thermal stability of $Nd_xSc_yZr_{1-x-y}O_{2-\delta}$
490 materials proposed for inert matrix fuel applications *Inorg. Chem.* (2016) **55**, 1032-1043.
491 55. R. Oberti, S. Quartieri, M.C. Dalconi, F. Boscherini, G. Iezzi, M. Boiocchi, S.G.
492 Eeckhout, Site preference and local geometry of Sc in garnets: Part I. Multifarious mechanisms
493 in the pyrope-grossular join *Am. Mineral.* (2006) **91**, 1230−1239.
494 56. P. Li, I.W. Chen, J.E. Penner-Hahn, T.Y. Tien, X-ray absorption studies of ceria with
495 trivalent dopants *J. Am. Ceram. Soc.* (1991) **74**, 956-967.
496 57. I.I. Mazin, A.I. Liechtenstein, O.V. Ivanov, Breathing instability and disproportionation
497 of Bi^{4+} ions in $BaBiO_3$. *Ferroelectr.* (1995) **164**, 169-175.
498 58. N. Jiang, J.C.H. Spence, Can near-edge structure of the Bi L_3 edge determine the
499 formal valence states of Bi? *J. Phys. – Condens. Matter* (2006) **18**, 8029-8063.

59. A. De Mourgues, C. Dussarrat, R. Bontchev, B. Darriet, F. Weill, J. Darriet, XRD, EXAFS, and XANES studies of new bismuth cubic or pseudo-cubic perovskite-type phases *Nucl. Instr. Meth. Phys. Res. B* (1995) **97**, 82-88.

7. Figures and Tables Caption

Figure 1. Representations of the three perovskite structures observed in the (1-*x*)$PbTiO_3$–*x*$BiScO_3$ and (1-*x*)$PbTiO_3$–*x*$BiScO_3$ solid solutions highlighting the Ti^{4+}/Sc^{3+} octahedron. The black arrow shows the direction of polarization in the tetragonal *P4mm* (*z*-direction) and rhombohedral *R3m* (<111> direction) perovskite structures. Note that the cubic $Pm\bar{3}m$ perovskite structure does not exhibit polarization.

Figure 2. The fitted XRD patterns of a) (1-*x*)$BaTiO_3$–*x*$BiScO_3$ ($0 \leq x \leq 0.4$) and b) (1-*x*)$PbTiO_3$–*x*$BiScO_3$ ($0 \leq x \leq 0.3$). The solid black lines represents the raw diffraction patterns and the solid red lines represents the results of the Rietveld refinements. The residual pattern is shown in blue. Results of the Rietveld refinements are tabulated in Table 1.

Figure 3. Plots of unit cell parameters as functions of *x* for a) (1-*x*)$BaTiO_3$–*x*$BiScO_3$ ($0 \leq x \leq 0.4$) and b) (1-*x*)$PbTiO_3$–*x*$BiScO_3$ ($0 \leq x \leq 0.3$). Black symbols correspond to the unit cell parameters of the tetragonal *P4mm* phase. Red symbols correspond to the unit cell parameters of the cubic $Pm\bar{3}m$ phase.

Figure 4. Enlargements of the XRD patterns of a) (1-*x*)$BaTiO_3$–*x*$BiScO_3$ ($0 \leq x \leq 0.4$) and b) (1-*x*)$PbTiO_3$–*x*$BiScO_3$ ($0 \leq x \leq 0.3$) highlighting the shifts in the (002) and (020) diffraction peaks.

Figure 5. The Ti K-edge XANES spectra of a) (1-*x*)$BaTiO_3$–*x*$BiScO_3$ and b) (1-*x*)$PbTiO_3$–*x*$BiScO_3$ solid solutions. The dashed line represents the Ti K-edge absorption edge energy and is used to visually separate the main edge (labelled A) and pre-edge (labelled B) regions. Major features of the Ti K-edge pre-edge region are highlighted in the inserts.

Figure 6. The Sc K-edge XANES spectra of a) (1-*x*)$BaTiO_3$–*x*$BiScO_3$ and b) (1-*x*)$PbTiO_3$–*x*$BiScO_3$ solid solutions. The dashed line represents the Si K-edge absorption edge energy and is used to visually separate the main edge (labelled A) and pre-edge (labelled B) regions. Major features of the Sc K-edge pre-edge region are highlighted in the insets.

Figure 7. The Bi L_3-edge XANES spectra of representative members of the a) (1-*x*)$BaTiO_3$–*x*$BiScO_3$ and b) (1-*x*)$PbTiO_3$–*x*$BiScO_3$ solid solutions. The Bi L_3-edge XANES spectra of Bi_2O_3 (Bi^{3+}) and Ba_2LuBiO_6 (Bi^{5+}) are displayed as the black dash and solid lines, respectively. Features A-C are discussed in the text. All spectra were collected in fluorescence mode.

Table 1. Results of the Refinements of (1-*x*)$BaTiO_3$–*x*$BiScO_3$ and (1-*x*)$PbTiO_3$–*x*$BiScO_3$.

Figures and Tables

Figure 1

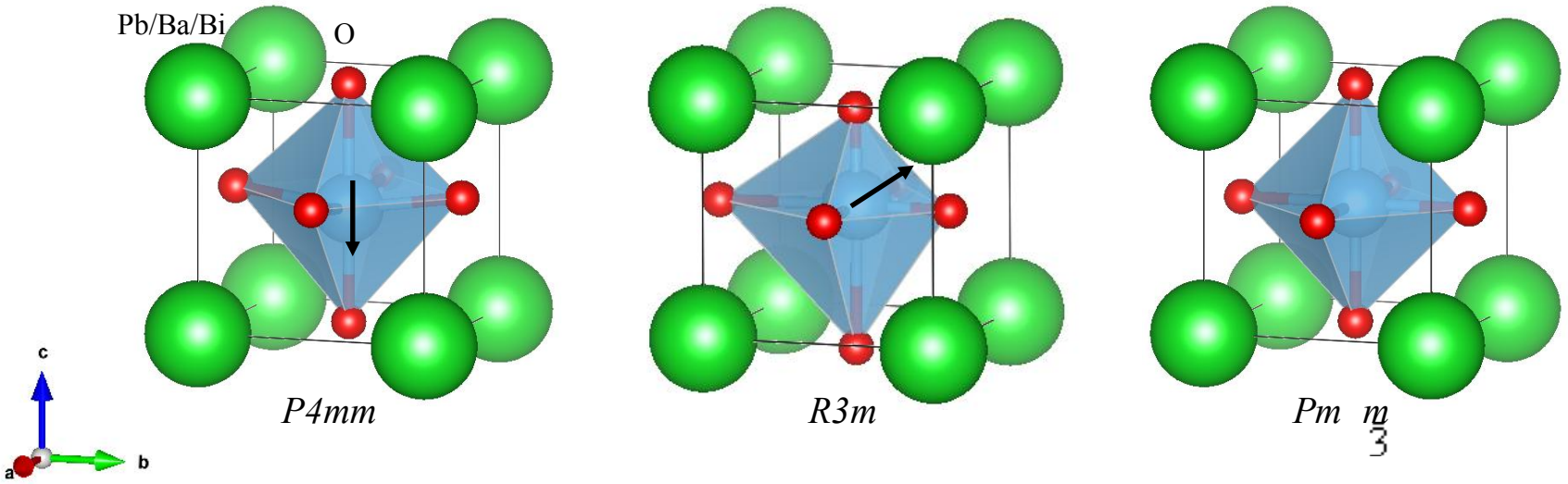

Figure 2.

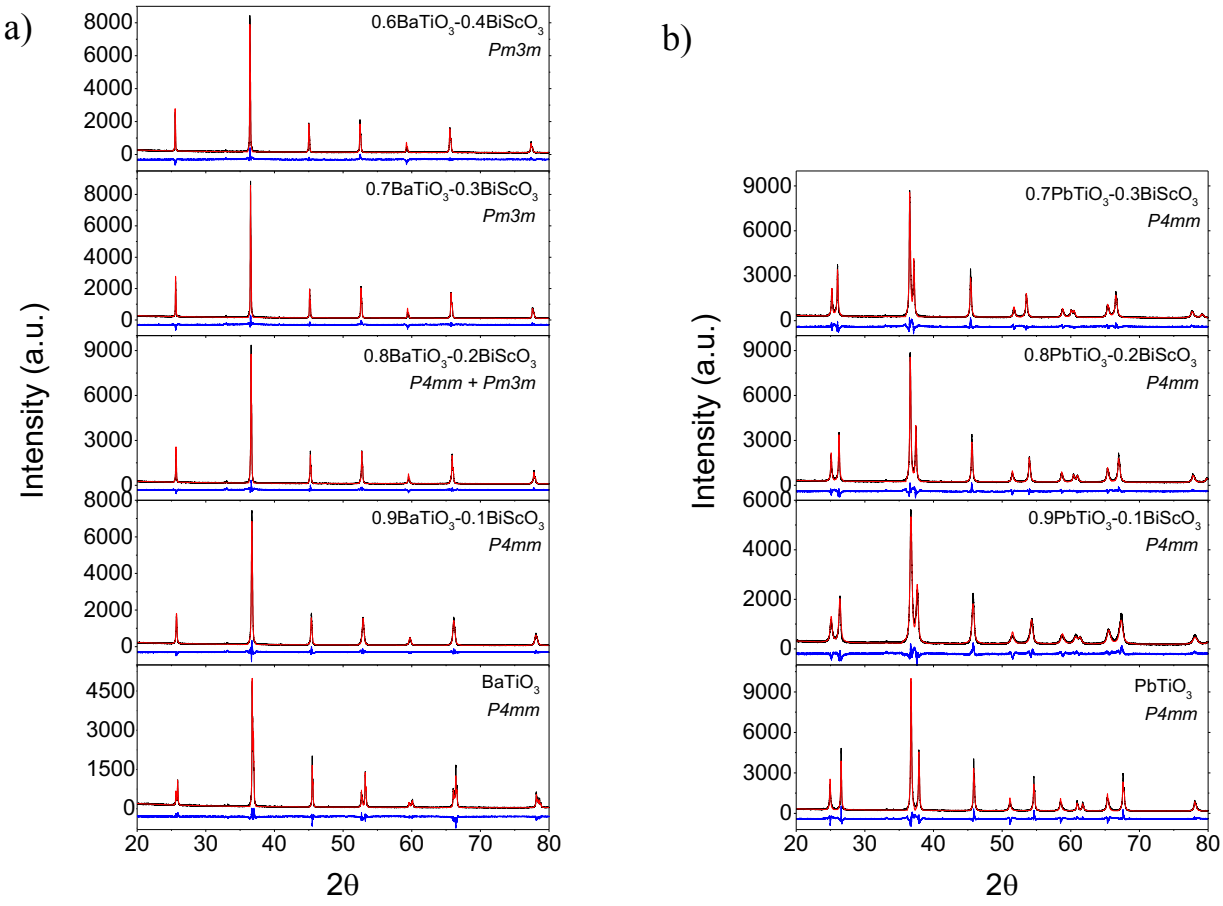
a)
b)
Intensity (a.u.)
2θ
0.6BaTiO3-0.4BiScO3
Pm3m
0.7BaTiO3-0.3BiScO3
Pm3m
0.8BaTiO3-0.2BiScO3
P4mm + Pm3m
0.9BaTiO3-0.1BiScO3
P4mm
BaTiO3
P4mm
0.7PbTiO3-0.3BiScO3
P4mm
0.8PbTiO3-0.2BiScO3
P4mm
0.9PbTiO3-0.1BiScO3
P4mm
PbTiO3
P4mm

Figure 3

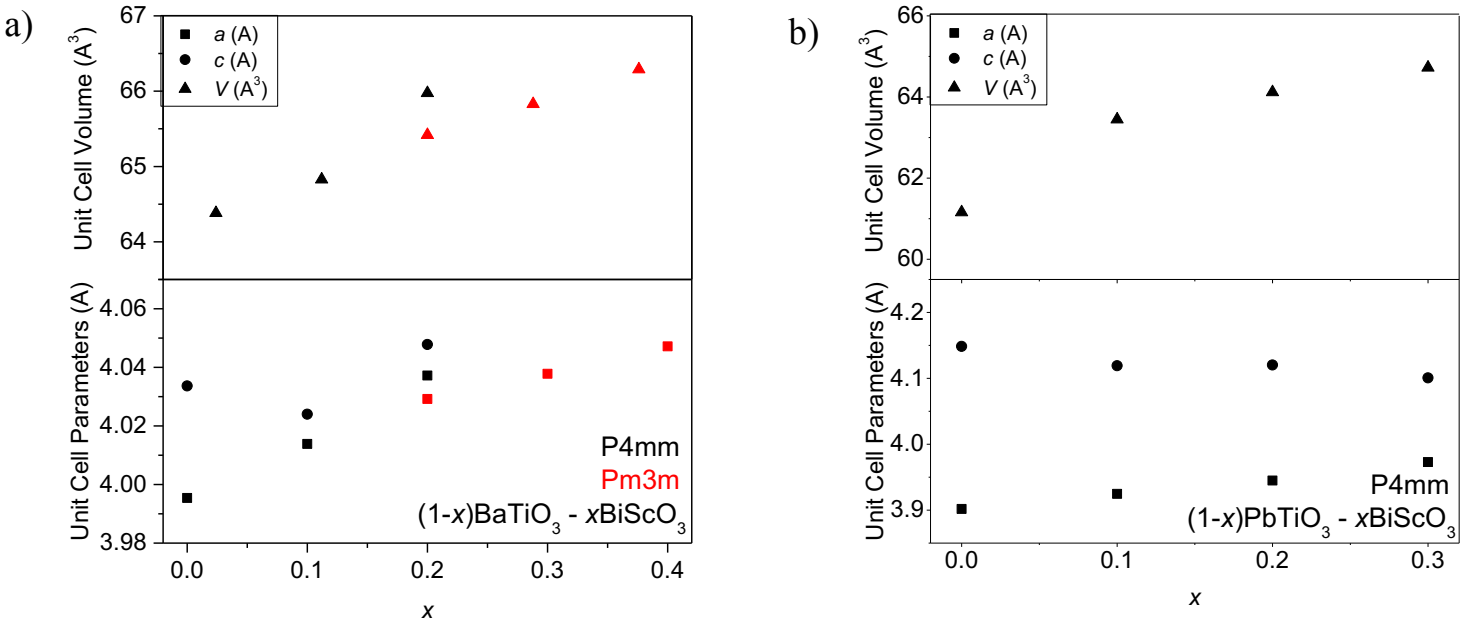
a)
a (A)
c (A)
V (A3)
Unit Cell Volume (A3)
Unit Cell Parameters (A)
P4mm
Pm3m
(1-x)BaTiO3 - xBiScO3
x
b)
a (A)
c (A)
V (A3)
Unit Cell Volume (A3)
Unit Cell Parameters (A)
P4mm
(1-x)PbTiO3 - xBiScO3
x

Figure 4

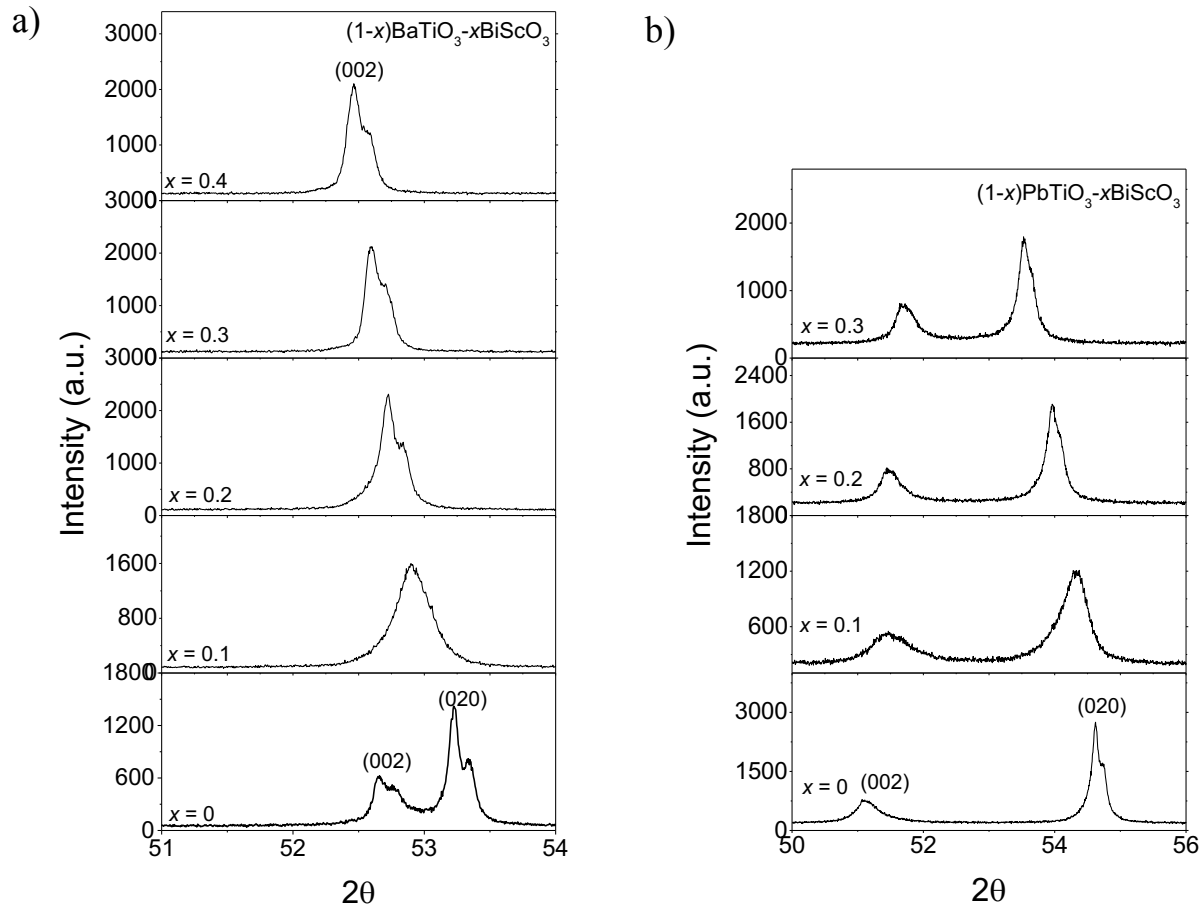
a)
(1-x)BaTiO3-xBiScO3
(002)
x = 0.4
x = 0.3
x = 0.2
x = 0.1
x = 0
(020)
(002)
Intensity (a.u.)
2θ
b)
(1-x)PbTiO3-xBiScO3
x = 0.3
x = 0.2
x = 0.1
x = 0
(020)
(002)
Intensity (a.u.)
2θ

Figure 5

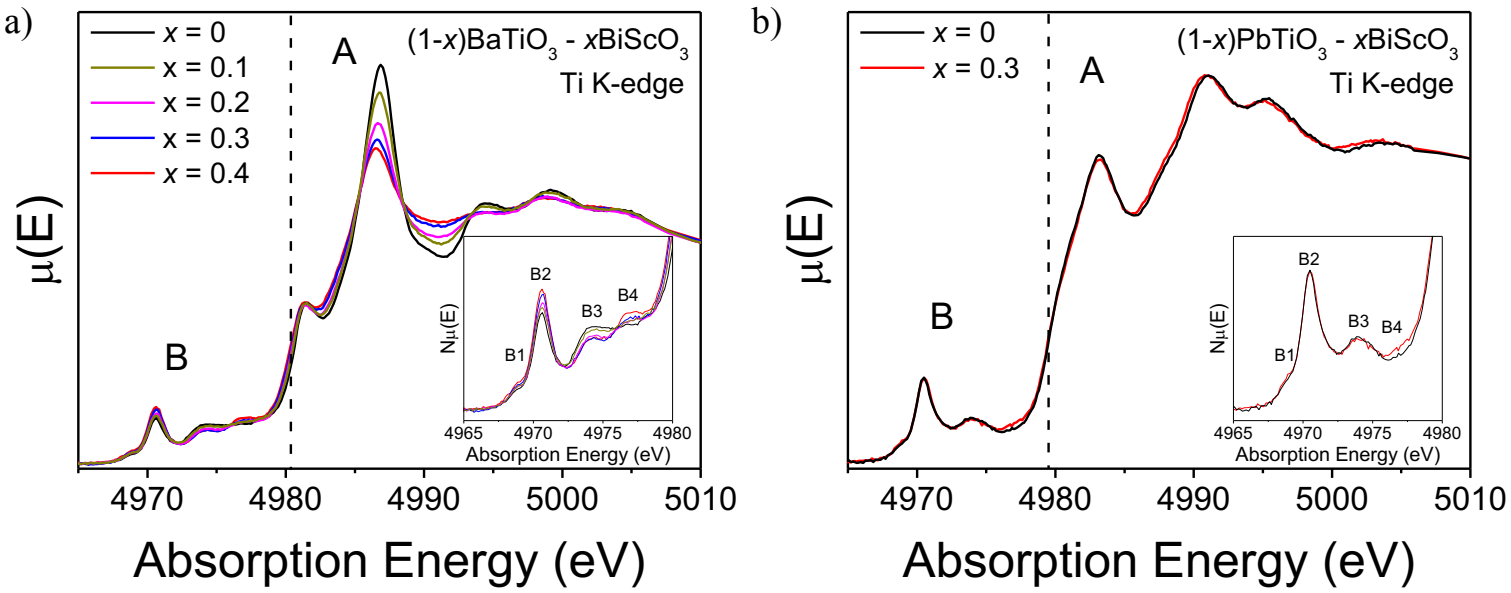
a)
x = 0
x = 0.1
x = 0.2
x = 0.3
x = 0.4
(1-x)BaTiO3 - xBiScO3
Ti K-edge
A
B
B1
B2
B3
B4
Nμ(E)
4965 4970 4975 4980
Absorption Energy (eV)
μ(E)
4970 4980 4990 5000 5010
Absorption Energy (eV)
b)
x = 0
x = 0.3
(1-x)PbTiO3 - xBiScO3
Ti K-edge
A
B
B1
B2
B3
B4
Nμ(E)
4965 4970 4975 4980
Absorption Energy (eV)
μ(E)
4970 4980 4990 5000 5010
Absorption Energy (eV)

Figure 6

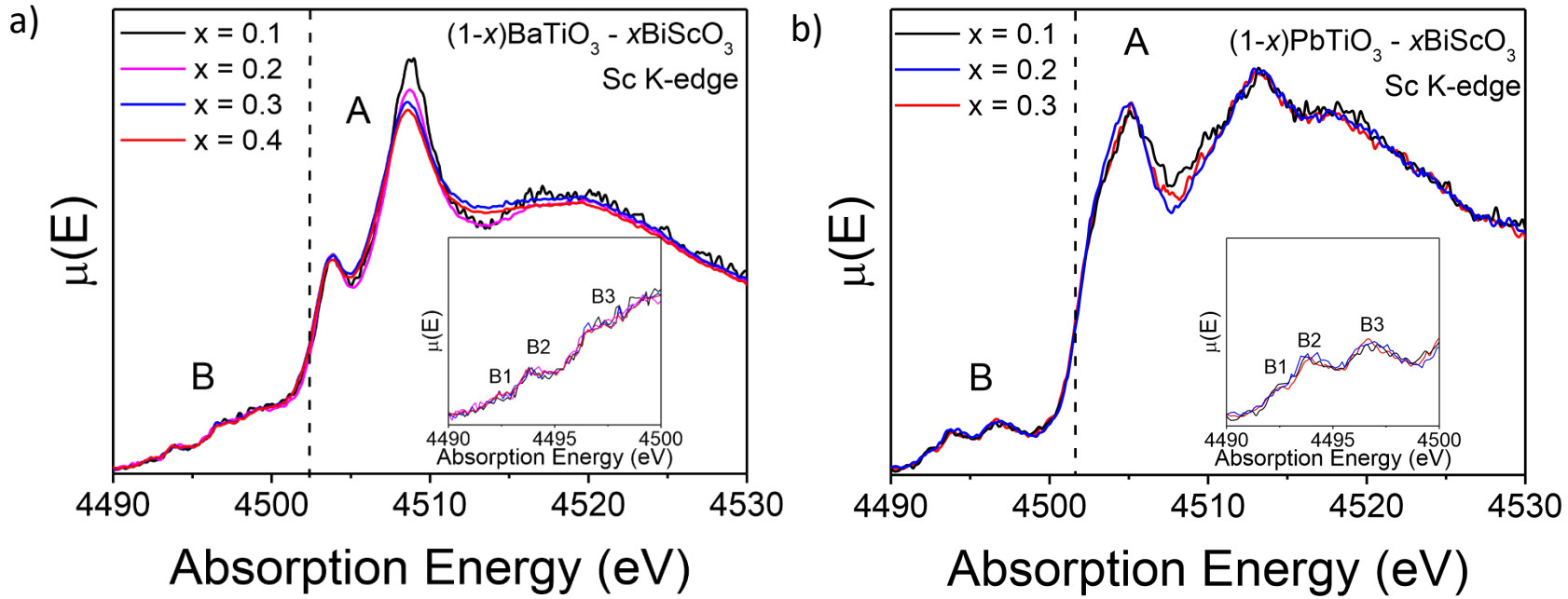
a)
x = 0.1
x = 0.2
x = 0.3
x = 0.4
(1-x)BaTiO3 - xBiScO3
Sc K-edge
A
B
B1
B2
B3
μ(E)
4490
4495
4500
Absorption Energy (eV)
4490
4500
4510
4520
4530
Absorption Energy (eV)
b)
x = 0.1
x = 0.2
x = 0.3
(1-x)PbTiO3 - xBiScO3
Sc K-edge
A
B
B1
B2
B3
μ(E)
4490
4495
4500
Absorption Energy (eV)
4490
4500
4510
4520
4530
Absorption Energy (eV)

Figure 7

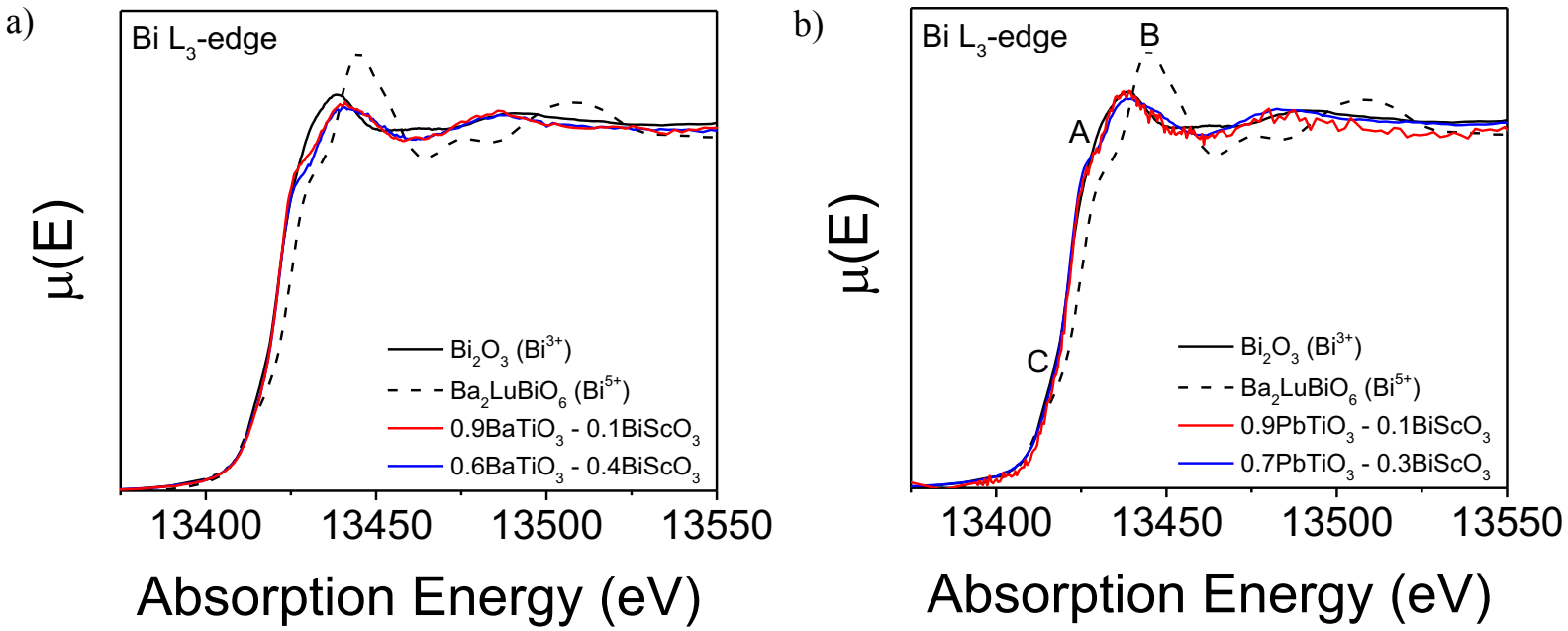
a)
Bi L3-edge
μ(E)
Bi2O3 (Bi3+)
Ba2LuBiO6 (Bi5+)
0.9BaTiO3 - 0.1BiScO3
0.6BaTiO3 - 0.4BiScO3
13400
13450
13500
13550
Absorption Energy (eV)
b)
Bi L3-edge
A
B
C
μ(E)
Bi2O3 (Bi3+)
Ba2LuBiO6 (Bi5+)
0.9PbTiO3 - 0.1BiScO3
0.7PbTiO3 - 0.3BiScO3
13400
13450
13500
13550
Absorption Energy (eV)

Table 1

	$(1-x)BaTiO_3$–$xBiScO_3$					$(1-x)PbTiO_3$–$xBiScO_3$			
	x = 0	x = 0.1	x = 0.2		x = 0.3	x = 0.4	x = 0	x = 0.1	x = 0.2	x = 0.2
Space Group	*P4mm* (No. 99)	*P4mm* (No. 221)	*P4mm* (No. 99)	$Pm\bar{3}m$ (No. 221)	$Pm\bar{3}m$ (No. 221)	$Pm\bar{3}m$ (No. 221)	*P4mm* (No. 99)	*P4mm* (No. 99)	*P4mm* (No. 99)	*P4mm* (No. 99)
X (%)	100 %	100 %	12.5 %	87.5 %	100 %	100 %	100 %	100 %	100 %	100 %
a (Å)	3.99524(5)	4.01383(7)	4.0372(1)	4.02918(3)	4.03779(4)	4.04715(4)	3.90109(6)	3.9242(1)	3.94484(6)	3.97294(7)
c (Å)	4.03364(5)	4.02400(9)	4.0478(1)				4.14751(7)	4.1199(1)	4.12003(6)	4.10081(8)
V ($Å^3$)	64.383	64.829	65.976	65.411	65.831	66.289	63.119	63.426	64.115	64.728
$B_{overall}$	0.109	0.283	0.455		0.940	1.14	0.309	0.584	0.781	0.988
t	1.062	1.046	1.031	1.031	1.016	1.001	1.019	1.008	0.997	0.9860
Ti(Sc) *z*[a]	0.488(4)	0.498(2)	0.499(9)				0.462(2)	0.476(2)	0.471(2)	0.476(2)
Ti(Sc)-O1 (Å)	1.926	1.990	2.02	2.015	2.019	2.204	1.723	1.640	1.684	1.675
Ti(Sc)-O1 (Å)	2.107	2.034	2.028				2.414	2.479	2.436	2.425
Ti(Sc)-O2 (Å)	2.017	2.007	2.019				2.028	2.013	2.045	2.058
Avg Ti(Sc)–O(Å)	2.016667	2.010333	2.022333	2.015	2.019	2.204	2.055	2.044	2.055	2.052667
Ba(Bi)-O1 (Å)	2.825	2.838	2.855	2.849	2.855	2.862	2.807	2.823	2.833	2.851
Ba(Bi)-O2 (Å)	2.710	2.817	2.824				2.586	2.601	2.565	2.562
Ba(Bi)-O2 (Å)	2.974	2.867	2.893				3.132	3.109	3.169	3.180
Avg Ti(Sc)–O (Å)	2.836333	2.840667	2.857333	2.849	2.855	2.862	2.841667	2.844333	2.855667	2.864333
R_p[b]	8.42	7.22	6.72	6.79	6.97	8.77	7.33	6.76	6.84	6.83
R_{wp}[c]	11.61	9.210	8.86		9.27	9.73	11.77	9.51	8.98	8.99
R_{exp}[d]	8.27	6.89	6.42		6.76	6.72	5.16	5.21	5.09	5.03
χ^2	1.97	1.63	1.73		1.87	1.96[e]	3.86	3.33	3.21	3.20

[a] Ti(Sc) cations occupy the *1b* site at (½, ½, *z*). The *z* parameter was refined for each composition.

[b] Profile Residual: $R_p = \sum_i (y_{C,i} - y_{o,i}) / \sum_i y_{O,i}$

[c] Weighted Profile Residual: $R_{wp}^2 = \sum_i w_i (y_{C,i} - y_{o,i})^2 / \sum_i w_i (y_{O,i})^2$

[d] Expected Residual: $R_{exp}^2 = N / \sum_i w_i (y_{O,i})^2$

[e] *A*- and *B*-site occupancy parameters were refined. Bi and Sc occupied 3.8% of the *B*- and *A*-sites, respectively.